Growth of Surface Analysis and the Development of Databases and Modeling Software for Auger-Electron Spectroscopy and X-ray Photoelectron Spectroscopy

C. J. Powell
Materials Measurement Science Division, National Institute of Standards and Technology, Gaithersburg, Maryland 20899-8370
cedric.powell@nist.gov

Abstract: A short overview is presented of the growth of surface analysis and, in particular, of X-ray photoelectron spectroscopy (XPS) during the past 25 years. Information is given on some of the National Institute of Standards and Technology (NIST) databases that have been developed for applications in XPS and Auger-electron spectroscopy (AES) and that have helped enable this growth. Information is also provided on three XPS-modeling products that help users obtain quantitative information for an increasing range of complex materials.

Introduction

Microscopy Today published a special issue on surface analysis in 2011 in which Vincent S. Smentkowski provided an overview of four methods of surface analysis [1]: Auger-electron spectroscopy (AES), X-ray photoelectron spectroscopy (XPS), time-of-flight secondary-ion mass spectrometry (ToF-SIMS), and low-energy ion scattering (LEIS), which is also known as ion-scattering spectroscopy (ISS). He summarized the principal analytical capabilities of each method (lateral resolution, sampling depth, detection limit, elements analyzed, and molecular information), while other authors in the special issue provided additional information on each technique and gave examples of applications. Since 2011 there has been continued development of each technique, and the use of XPS has grown significantly relative to the other surface analysis methods. The growth in use of XPS has been driven by many factors including the availability of useful databases and modeling software.

Surface-sensitive tools have become increasingly important for a number of technologies because compositional information is now sought on smaller and smaller length scales. For the semiconductor industry, in particular, layer thicknesses are now so thin that there is little distinction between the surface or interface region and the bulk of the film [2]. A semiconductor or a display device consists of many layers, and information is often required of the film stability and of chemical interactions between layers. Similar information is required of nanomaterials and nanoparticles [3]. Surface analysis, often in combination with transmission electron microscopy (TEM) and other methods, can provide useful information on the local compositions of complex morphologies. The reader is referred to several books for further guidance on AES, XPS, ToF-SIMS, and LEIS [4–6].

In this article information is provided on some of the National Institute of Standards and Technology (NIST) databases that have been developed for applications in AES and XPS. Several types of XPS modeling software are described, and two examples are presented of the NIST Database for the Simulation of Electron Spectra for Surface Analysis (SESSA). The SESSA database can be used to simulate AES and XPS spectra for user-specified materials (multilayer thin-film samples and nanostructures such as islands, lines, spheres, and layered spheres on surfaces) and measurement conditions.

Growth of Surface Analysis

Figure 1 shows the numbers of published AES, SIMS, and XPS papers published per year from 1991 through 2015 based on a Web of Science search using their acronyms and key phrases. Two sets of AES publication data are included in Figure 1: one based on the use of "AES" in the search and the other without this term. The former data set is an overcount (because AES is also an abbreviation for atomic emission spectroscopy), while the latter data set is an undercount (because some Auger papers with AES in the title or abstract would be missed). Nevertheless, it appears from Figure 1 that the number of Auger papers published per year is roughly constant or slowly decreasing, while the corresponding number of SIMS papers is slowly increasing. We have not included LEIS data in Figure 1 because the number of publications with this method is relatively small.

Figure 1 clearly indicates that there has been a much larger growth in the number of XPS publications per year than for AES or SIMS. The XPS growth has been driven by a number of factors:

1. The wide diversity of specimen materials that can be analyzed by XPS
2. Improved methods for specimen handling and treatments
3. Novel and improved X-ray monochromators, electron energy analyzers, and detectors
4. Improved methods of charge control on non-conducting samples
5. Improved methods for thin-film analysis using cluster-ion sources and angle-resolved XPS
6. Improved software for instrument setup, data acquisition, and data analysis
7. Improved reliability of XPS analyses (instrumental calibrations, stability checks, improved procedures, physical data, and information on specimen morphology)
8. Availability of advanced modeling software
9. Imaging of chemical species (either laterally or as a function of depth)
10. Improved analyses at "ambient" pressures
11. Use of synchrotron radiation (for example, for varying surface/bulk sensitivity by changing the X-ray energy and thus the photoelectron energy for a given core level to obtain a desired inelastic mean free path in the sample material)
12. Advanced materials for applications such as energy technologies, semiconductor devices, optoelectronics, magnetic-storage media, coatings, sensors, artificial joints, and implants in the human body

Revolutionize Your Confocal Imaging
ZEISS LSM 8 Family with Airyscan

The new LSM 8 family with Airyscan will revolutionize your confocal imaging.
Acquire better images with higher signal and less noise. Gain superresolution, 1.7x over traditional confocal. Image faster and acquire more data in less time for higher throughput.

Choose LSM 880 with Airyscan for large labs or imaging facilities with diverse samples and/or multiphoton application needs. Or select LSM 800 with Airyscan for an economical confocal system that provides the same amazing imaging and superresolution for smaller facilities and individual labs.

https://doi.org/10.1017/S1551929516000080 Published online by Cambridge University Press

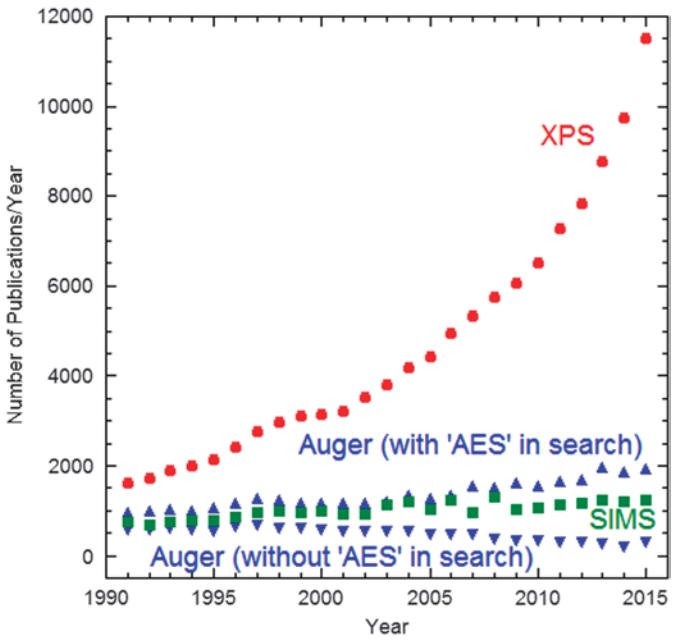

Figure 1: Plot of numbers of papers published per year on AES, SIMS, and XPS from 1991 through 2015 based on a Web of Science search using acronyms and key phrases for these techniques.

13. Nanoscience and nanotechnology for applications such as semiconductor devices, composites, and drug-delivery systems

The publication plots in Figure 1 cannot, of necessity, represent the many unpublished practical applications of each technique (for example, from industrial laboratories) or the economic impacts of these applications. Nevertheless, Figure 1 shows that XPS and its applications are of growing significance and are a major component of the growth in surface analysis.

NIST Databases for AES and XPS

NIST has developed seven databases to advance quantitative applications of AES and XPS [7]:

- NIST X-ray Photoelectron Spectroscopy Database (SRD 20)
- NIST Electron Elastic-Scattering Cross-Section Database (SRD 64)
- NIST Electron Inelastic-Mean-Free-Path Database (SRD 71)
- NIST Electron Effective-Attenuation-Length Database (SRD 82)
- NIST Database for the Simulation of Electron Spectra for Surface Analysis (SESSA) (SRD 100)
- NIST Backscattering-Correction-Factor Database for Auger Electron Spectroscopy (SRD 154)
- NIST Database of Cross Sections for Inner-Shell Ionization by Electron or Positron Impact (SRD 164)

The short descriptions below highlight applications of some of these databases that may be of interest to the microscopy community.

SRD 20. This online database is a useful resource for core-electron binding energies and for the changes in these binding energies with change of chemical state. This information could be useful in interpretations of electron energy-loss spectra in TEM. The database also provides information on Auger-electron energies for Auger transitions that are commonly observed with XPS spectra acquired using Mg Kα and Al Kα X-ray sources. Changes in Auger energies with change of chemical state are also available.

SRD 64. This database provides differential elastic-scattering cross sections, total elastic-scattering cross sections, phase shifts, and transport cross sections for elements with atomic numbers from 1 to 96 and for electron energies between 50 eV and 300 keV (in steps of 1 eV). These cross sections can be used in calculations of electron transport for quantitative AES, XPS, electron probe microanalysis (EPMA), analytical electron microscopy (AEM), lithography, and radiation dosimetry.

SRD 71. The material parameter that is most important for determining the surface sensitivity of AES and XPS is the inelastic mean free path (IMFP), which depends both on material and electron energy [8]. For energies between 50 eV and 2 keV, the range of practical interest for most AES and XPS applications, the IMFP varies from about 0.4 nm to about 6 nm [8]. While SRD 71 contains IMFPs needed for the AES and XPS energy range, Shinotsuka et al. [9] have recently calculated IMFPs in 41 elemental solids for energies up to 200 keV. Figure 2 shows a comparison of their IMFPs for 32 elemental solids and corresponding measured IMFPs for energies of 100 keV and 200 keV where, apart from Be, there is excellent correlation [9]. Shinotsuka et al. also found that a relativistic extension of the IMFP predictive formula designated TPP-2M, developed initially for AES and XPS [8], was useful up to 200 keV. The new IMFPs and the TPP-2M formula should thus be useful for film-thickness measurements by electron energy-loss spectroscopy in the TEM.

SRD 100. This database contains extensive physical data needed for quantitative interpretations of AES and XPS data. It can also be used to simulate AES and XPS spectra for planar multilayer films and for nanostructures such as islands, lines, spheres, and layered spheres on surfaces. Some examples of SESSA simulations will be given in the following section.

SRD 164. This database provides calculated cross sections for ionization of the K shell, and of the L and M subshells, of atoms by electron impact from the ionization threshold to 1 GeV. Extensive comparisons have been made of these cross sections with measured cross sections that satisfied mutual-consistency checks [10]. These comparisons showed that the overall root–mean–square deviation between the calculated and measured cross sections was 10.9 %. The calculated cross sections should be useful in calculations of X–ray yields in EPMA and AEM amongst other applications.

NIST also has an online database for X-ray transition energies (K- and L-series lines) [11] and three databases for X-ray absorption coefficients (developed for different purposes) [12].

Modeling Software for AES and XPS Applications

Most AES and XPS analyses are based on the simplifying assumptions that the samples of interest are homogeneous over the sampling depths of the measurements and that the sample surfaces are flat over the analysis area. The first assumption is usually incorrect even for flat samples because they may contain multiple phases such as one or more thin-film layers as well as surface contamination. For example, the intensity of

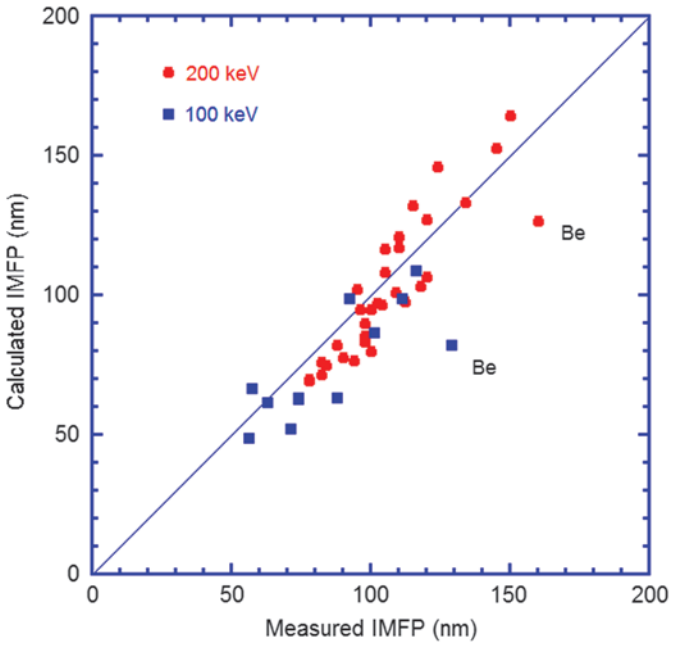

Figure 2: Comparison of inelastic mean free paths (IMFPs) calculated by Shinotsuka et al. with corresponding measured IMFPs for 11 elemental solids at 100 keV and for 32 elemental solids at 200 keV [9]. The solid line indicates perfect correlation between the calculated and measured IMFPs. Good correlations between calculated and measured IMFPs are found except for Be.

a substrate photoelectron line will change considerably following deposition of an overlayer film of increasing thickness. Information about possible variations of sample composition with depth can be obtained from comparisons of XPS spectra for two different electron-emission angles (for example, at 0° and 60° with respect to the surface normal). If the ratio of these spectra is close to unity over the energy range for the photoelectron peaks of interest, the sample is homogeneous over the XPS sampling depth [8]; otherwise, there is depth inhomogeneity. Information on possible lateral inhomogeneities can be obtained from imaging AES or XPS instruments. Quantitative analyses of samples that may have a variety of shapes (for exmaple, nanoparticles and fibers) can be modeled in several ways including use of the software tools discussed here. It is therefore necessary for an analyst to identify the sample morphology before attempting a quantitative analysis from observed peak intensities.

We now briefly describe three XPS-modeling software products that have been developed to provide insights on morphological effects, to identify certain types of morphologies, and to relate structural models of a sample to spectral data. We show two examples of the use of SRD 100 (SESSA) for obtaining more quantitative information about a sample and for estimating XPS detection limits for thin-film samples.

XPS Multiquant. Mohai [13] has described software that can be used to simulate photoelectron peak intensities for various types of sample morphologies (planar films; layers on planar films, spheres, and cylinders; islands on planar films, spheres, and cylinders; and layers on polyhedra and nanotubes). The peak intensities can be calculated using various options for parameter values (such as IMFPs and photoionization cross sections). Users can choose to manually adjust parameters such as film thickness or to use a fitting program that can optimize the agreement of calculated peak intensities with measured peak intensities.

QUASES. Tougaard [14–16] has developed theory and the associated QUASES software for simulating photoelectron peaks and their associated inelastic tails in XPS. He showed that the overall spectral shape (that is, peaks and their inelastic tails) depended greatly on the assumed sample morphology. In a now-classic example, he showed model spectra with identical Cu $2p_{3/2}$ peak intensities that were obtained from four Cu/Au samples with very different distributions of Cu with depth. The top row in Figure 3 shows schematic representations of the four Cu/Au morphologies considered by Tougaard: (a) a 0.11 nm Cu film on an Au substrate, (b) a 5 nm $CuAu_4$ alloy on an Au substrate, (c) a 1 nm Cu film buried 2 nm deep in an Au matrix, and (d) a 2.5 nm Au film on a Cu substrate [14]. These particular morphologies were chosen to given identical Cu $2p_{3/2}$ peak intensities in the simulated Cu 2p spectra shown in the bottom panel of Figure 3. Although the peak Cu $2p_{3/2}$ intensities were the same for each morphology, the samples had very different amounts of Cu in the near-surface region of each sample.

Tougaard's QUASES software [15] enables a user to compare a measured spectral shape for a particular photoelectron peak with a simulated shape for a particular morphology. The user can then decide whether or not a particular morphology provides satisfactory agreement of the spectral shapes. If agreement is obtained, quantitative data may be acquired on the depth and thickness of a buried film or the dimensions of islands on a surface. Numerous studies have now been performed that show consistency between results of analyses with QUASES and with other methods [15]. Tougaard has also developed more-approximate algorithms for automated processing of the thousands of spectra that may be acquired for the pixels in an XPS image [15].

SESSA. The NIST SESSA database (SRD 100) [16,17] was designed to facilitate quantitative interpretations of AES and XPS spectra and to improve the accuracy of quantitation in routine analysis. The SESSA database contains the physical data for quantitative interpretation of a measured spectrum (for example, IMFPs, differential inverse IMFP with respect to energy loss, differential and total elastic–scattering cross sections, photoionization cross sections and asymmetry parameters for XPS, electron–impact ionization cross sections, fluorescence yields (from which Auger yields are determined), and backscattering factors for AES).

Spectra can be simulated with SESSA by an efficient Monte Carlo engine for a measurement configuration specified by the user and for a specimen morphology selected by the user. These simulations can be performed for one or more films on a planar substrate, as indicated by the schematic in Figure 4. For this application, a user specifies the composition and thickness of each film and the substrate composition. SESSA can also be used to simulate AES and XPS spectra of various types of nanostructures such as islands, lines, spheres, and layered spheres on a substrate. In this case, a user specifies the composition and dimensions of each type of nanostructure as well as the substrate composition. Figure 5 shows a schematic representation of core-shell nanoparticles on a substrate. The nanostructures in SESSA are considered to exist in a rectangular

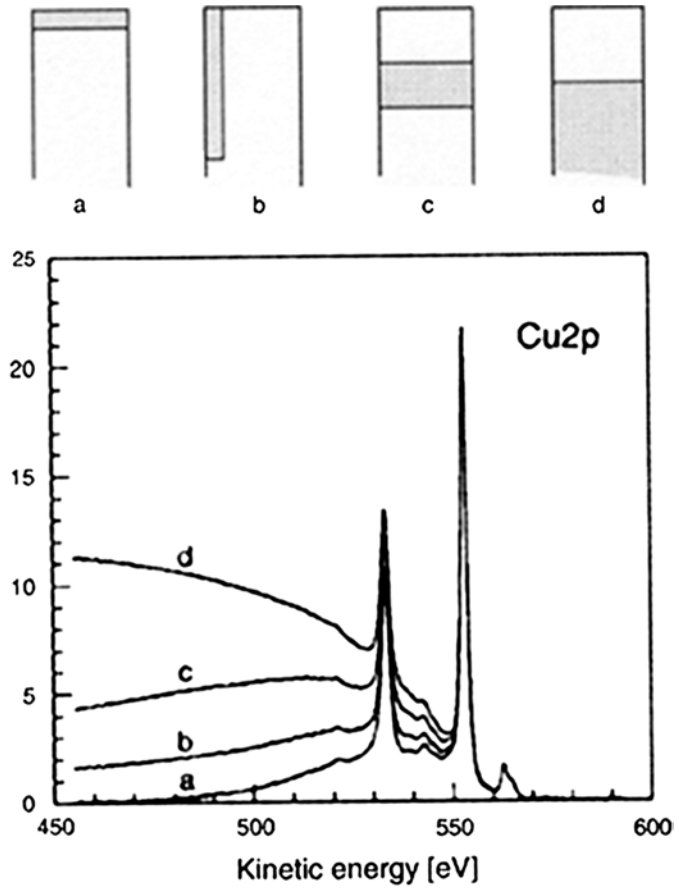

Figure 3: Top: Schematic representation of four different Cu/Au samples with (a) a 0.11 nm Cu film on an Au substrate; (b) a 5 nm $CuAu_4$ alloy on an Au substrate; (c) a 1 nm Cu film buried 2 nm deep in an Au matrix; and (d) a 2.5 nm Au film on a Cu substrate. Bottom: Simulated Cu 2p spectra for the four Cu/Au samples shown at top. Reproduced with permission from S Tougaard, *J Vac Sci Technol A* 14 (1996) 1415. Copyright 1996, American Vacuum Society.

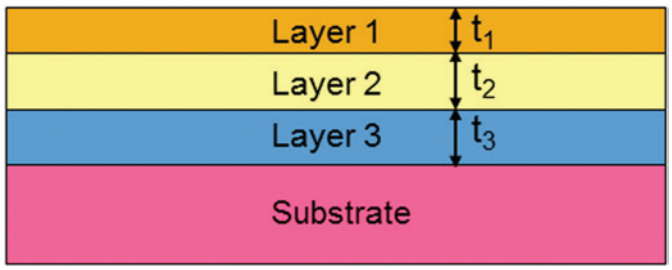

Figure 4: Schematic representation of three films of different compositions and with thicknesses t_1, t_2, and t_3 on a planar substrate that can be used for simulations of an AES or XPS spectrum with the SESSA software [16, 17].

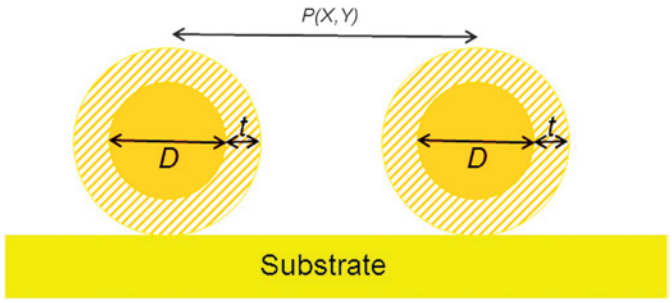

Figure 5: Schematic representation of core-shell nanoparticles, each defined by a core material with a diameter *D* and a shell material of thickness *t*, on a substrate with periodicities *P*(*X*,*Y*) in the *X* and *Y* directions. Morphologies of this type (and with additional shells) can be used for simulations of an AES or XPS spectrum with the SESSA software [16, 17].

array on the substrate, and the user specifies the periodicity (that is, the separation of the nanostructures) in both the *X* and *Y* directions on the substrate surface.

Examples of the use of SESSA for nanoparticle characterization with XPS are given in the paper by Yung-Cheng Wang et al. in this issue. In this and other examples, simulated spectra from SESSA can be compared with measured spectra, and adjustments can be made to compositions and dimensions in SESSA as needed in order to find mutual consistency. We will now show two examples of SESSA applications that enable an analyst to obtain quantitative concentrations of surface impurities and to determine detection limits for thin-film samples.

Results

Analysis of multiple planar layers. Multi-layer mirrors (MLMs) are now used in extreme ultraviolet (EUV) lithography to provide maximum reflectivity at the operating wavelength (13.5 nm). These mirrors typically consist of about 50 bilayers, each consisting of about 4.3 nm Si and 3 nm Mo, on a Si substrate. The mirrors studied here were capped by a Ru layer with a thickness of about 3 nm to protect the optics from EUV-induced oxidation. The Ru surface is assumed to have a very thin native oxide (RuO_2). These MLM stacks were exposed to outgas contamination from EUV resists that may deposit submonolayer amounts of surface impurities such as N, P, S, and halogens such as F, Cl, Br. The samples also have a carbonaceous contamination layer on their surfaces from exposure to the atmosphere prior to XPS analysis. X-ray photoelectron spectroscopy has been used to detect the surface impurities, but it has been difficult to determine the absolute quantities of each impurity for correlation with reflectivity loss [18].

Figure 6 shows a wide-scan XPS spectrum (blue dots) and the corresponding SESSA simulation (red dots) for the conditions of the XPS measurement [18]. The measured spectrum shows weak peaks due to N and F as well as the expected peaks of Ru, C, O, Mo, and Si. The SESSA simulation was performed for a sample consisting of an outermost 0.25 nm layer of $CN_{0.02}F_{0.02}$ on 0.25 nm C, 0.25 nm RuO_2, 3 nm Ru, 4.3 nm Si, and 3 nm Mo on a Si substrate. The simulated spectrum was multiplied by the transmission function of the XPS instrument (an energy-dependent function that describes the relative efficiency with which photoelectrons are detected for given instrumental settings) and then normalized to the measured spectrum at a binding energy of 390 eV. While the simulated spectrum provides a reasonable match to the measured spectrum, there are some obvious differences. It was assumed, for simplicity in the simulations, that the XPS peaks had Lorentzian lineshapes. It was also assumed that a single differential inverse IMFP for Ru was applicable to all layers of the sample. It is sufficient, however, to recognize that N and F are surface impurities and that their XPS peaks appear on a slowly varying inelastic background associated with the other atoms in the sample. That is, the relative intensities of the N and F peaks compared to this background do not materially depend on the thicknesses of the other layers.

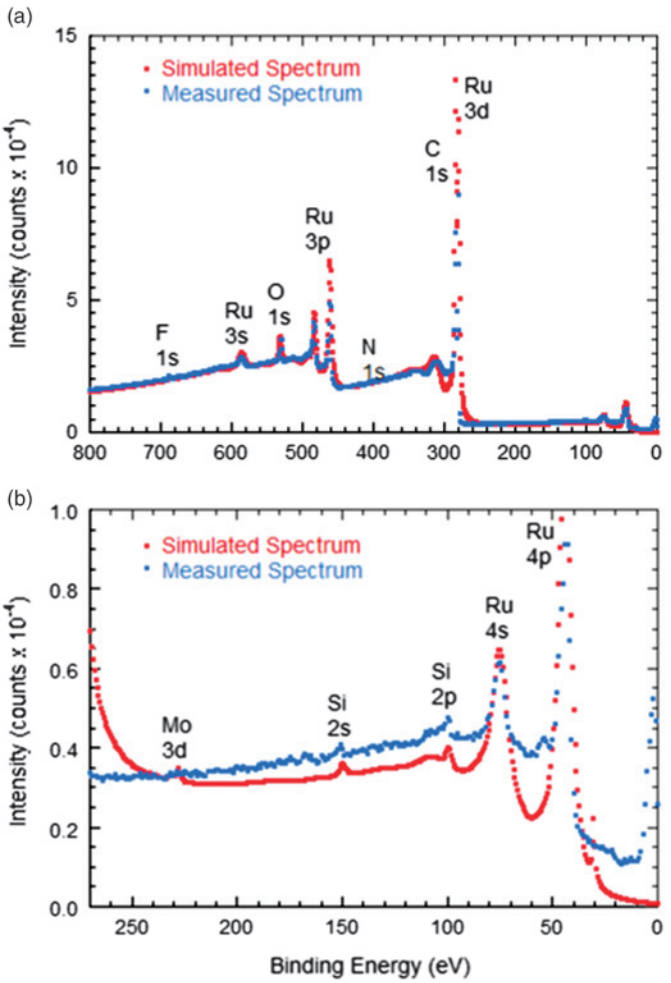

Figure 6: Comparison of measured (blue dots) and simulated (red dots) XPS spectra for a test multi-layer mirror of the type used for extreme-ultraviolet lithography [18]. (a) Binding energy to 800 eV, (b) expanded view of binding energies to 250 eV (see text for details).

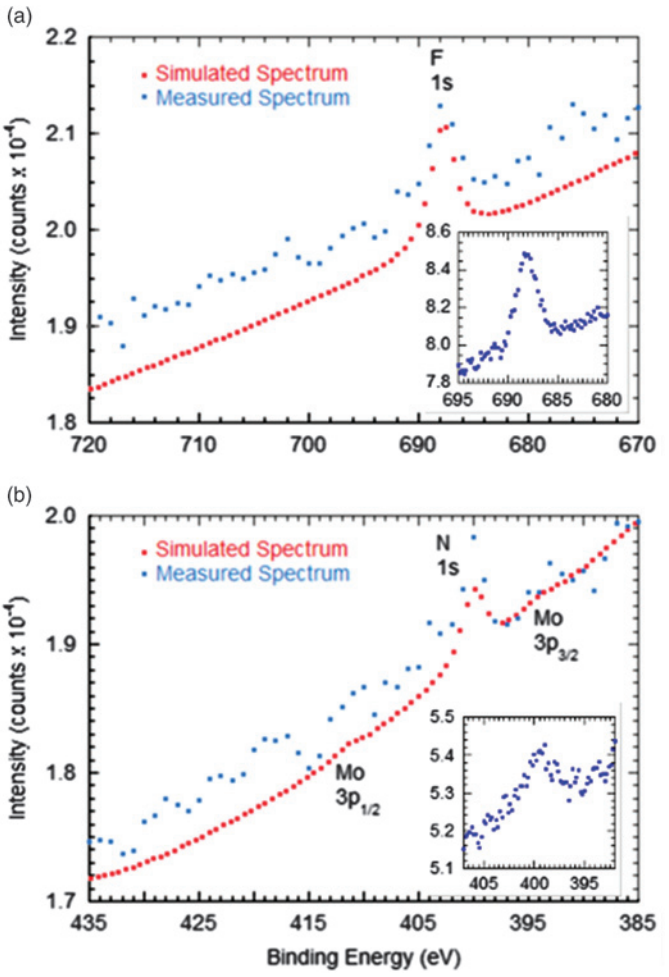

Figure 7: Comparison of measured (blue dots) and simulated (red dots) XPS spectra for the sample of **Figure 6** in the regions of (a) the F 1s peak and (b) the N 1s peak [18]. The insets show narrow-scan spectra for the F 1s and N 1s peaks (see text for details).

Figure 7 shows expanded views of Figure 6 in the regions of the F 1s and N 1s peaks [18]. As expected from the example of the simulated Cu 2p spectrum for a 0.11 nm Cu film on an Au substrate (morphology (a)) in Figure 3, there are no inelastic features on the low-energy sides of the F 1s and N 1s peaks in Figure 7 because F and N are surface impurities. Linear backgrounds were fitted to the spectra on both sides of the peaks and subtracted from the spectra. Comparisons of the resulting peak areas indicated that the surface layer on the test MLM sample contained 0.01 of a monolayer (ML) of F and 0.03 of a ML of N. The standard deviations of these surface concentrations were relatively large, 23% and 27%, respectively, because the peak areas were each determined from a wide-scan spectrum with relatively poor counting statistics. Narrow-scan spectra with improved counting statistics and additional points defining each peak were also recorded, as shown in the insets of Figure 7, and the standard deviations of the measured peak areas were reduced to 4% and 9%, respectively [18]. There was also an estimated one-standard-deviation systematic uncertainty in the peak intensities from the SESSA simulations of about 13% [18]. With the procedures outlined in [18], an XPS analyst can optimize the data–acquisition times needed to obtain a given uncertainty in an absolute surface concentration.

Detectability of a surface layer or a buried thin film. Our second SESSA example concerns XPS detection limits for a thin film on or buried in a chosen solid [19]. The bottom curve in Figure 8 is a simulated XPS spectrum for a homogeneous $RuW_{0.001}$ alloy with Al Kα X-rays incident at an angle of 55° (with respect to the surface normal) and for a photoelectron emission angle, α, of 0°, also with respect to the surface normal [19]. The middle and top curves in Figure 8 show the same spectrum multiplied by factors of 10 and 100, respectively. The $RuW_{0.001}$ alloy was selected as a convenient example for demonstrating the relatively favorable case for detection of the W $4d_{5/2}$ peak on the weak Ru background at the binding energy for the W peak. In such cases, the XPS detection limit is believed to be around 0.1 at. % [4–6]. We see that the weak W $4d_{5/2}$ peak is barely detectable by eye in the middle curve of Figure 8 but is more prominent in the top curve.

Simulations were then made for a thin W film of thickness t on a Ru substrate and for W films of varying thicknesses, t, at different depths, z, in a Ru matrix [19]. In each case, the value of t was adjusted so that the W $4d_{5/2}$ peak intensity was within 1% of the value for the $RuW_{0.001}$ alloy, as shown in Figure 8. A similar set of simulations was made for $\alpha = 55°$ and for normal X-ray incidence. It was convenient to express the derived film

thicknesses in terms of the equivalent number of W monolayers. The average atomic spacing, a, for a solid is given by

$$a^3 = 10^{21}\, M/(\rho N_A), \text{ (in nm}^3\text{)} \quad (1)$$

where M is the atomic or molecular weight of the solid, ρ is the density (in g/cm^3), and N_A is the Avogadro constant. For W, a = 0.251 nm. It was also convenient to express the depth of the buried W film in terms of λ_i, the IMFP of the W 4d$_{5/2}$ photoelectrons in the Ru matrix (1.79 nm at a kinetic energy of 1243 eV [19]). All depths were measured with respect to the upper surface of the W film; that is, these depths correspond to the varying thicknesses of the Ru overlayer.

Figure 9 shows plots of $t/(a\cos\alpha)$ as a function of $z/(\lambda_i\cos\alpha)$ for W 4d$_{5/2}$ photoelectrons in the Ru matrix when $\alpha = 0°$ and $\alpha = 55°$ [19]. These plots show, as expected, that larger W film thicknesses are needed for detectability of a given W 4d$_{5/2}$ peak intensity at larger depths of the W film in the Ru matrix. For $(z/\lambda_i\cos\alpha) = 0$, we see that approximately 0.006 ML of W is detectable on the Ru substrate for our assumed conditions. That is, 0.006 ML of W on the Ru surface provides the same W 4d$_{5/2}$ peak intensity as that shown in Figure 8 for the RuW$_{0.001}$ alloy. For $(z/\lambda_i\cos\alpha) = 4$, however, approximately 1.5 ML of W is needed for detectability at this depth (that is, for observing the same 4d$_{5/2}$ peak intensity as shown in Figure 8). For larger depths of the W film, there is greater scatter of the points because there is a larger range of film depths that (statistically) give similar W 4d$_{5/2}$ peak intensities.

The semi-logarithmic plots in Figure 9 were chosen because we expect, in the assumed absence of elastic scattering of the detected photoelectrons, that the photoelectron intensity from a buried thin film would depend exponentially on the thickness of the overlayer film (that is, the depth z) and inversely on the cosine of the emission angle, α. It is also reasonable that the thickness of the buried film, t, should depend on the cosine of the emission angle. The plots in Figure 9 are close to linear for values of $(z/\lambda_i\cos\alpha)$ from 0 to 4 when $\alpha = 0°$ and from 0 to about 6 when $\alpha = 55°$. Straight-line fits were made for each set of data, as indicated by the dashed lines in Figure 9. The results in Figure 9 indicate that SESSA simulations provide a convenient means of determining detection limits for surface films or buried layers in a matrix based on known or estimated detection limits for a homogeneous solid.

Discussion

Although XPS is regarded as a mature analytical technique increasingly used for a wide range of applications, these instruments can be applied in a variety of modes, and it may not be obvious how to use them effectively and efficiently for a wide range of samples, particularly by inexperienced operators. The over-simplified model of a homogeneous flat sample that is commonly used does not provide the complete information that can be extracted from XPS data for inhomogeneous samples (for example, compositional variations with depth or film thicknesses) or for nanostructured materials (for example, shell thicknesses of core-shell nanoparticles). The application of appropriate models for a sample can help analysts avoid pitfalls in practical analyses that may be associated with sample inhomogeneities, sample shape, instrument and software complexity, and the many options and procedures for data analysis. A workshop was held in 2002 to discuss the structure and initial content of a possible future expert system for XPS [20]. These discussions led to many recommendations concerning instrument and sample characterization, experimental objectives, instrument setup, acquisition and analysis

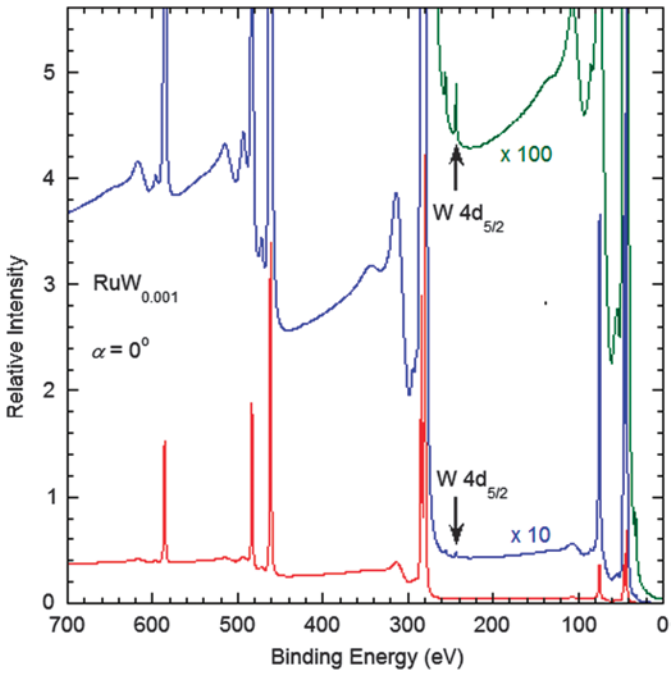

Figure 8: The bottom curve shows the simulated spectrum for a homogeneous RuW$_{0.001}$ alloy and a photoelectron emission angle, $\alpha = 0°$ [19]. The middle curve is this spectrum multiplied by a factor of 10, and the upper curve is the spectrum multiplied by a factor of 100. The vertical arrows mark the position of the W 4d$_{5/2}$ peak. The RuW$_{0.001}$ alloy composition was chosen because the XPS detection limit is expected to be about 0.1 at. % for the detection of the W 4d$_{5/2}$ peak on the nearby weak Ru background.

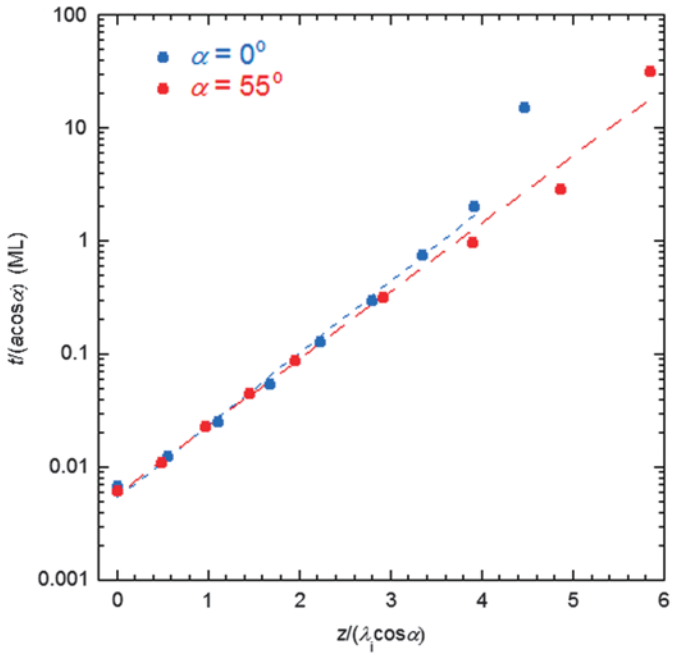

Figure 9: Plot of $t/(a\cos\alpha)$ expressed in units of monolayers (MLs) for thin films of W of thickness t on or in a Ru matrix as a function of $z/(\lambda_i\cos\alpha)$ for $\alpha = 0°$ (blue dots) and $\alpha = 55°$ (red dots) where a is the average W atomic spacing from Equation (**1**), λ_i is the IMFP of W 4d$_{5/2}$ photoelectrons in Ru, z is the depth of the W film, and α is the photoelectron emission angle with respect to the surface normal [19]. For each selected value of z, the value of t was adjusted until the W 4d$_{5/2}$ peak intensity was the same (within 1%) of the value found for the RuW$_{0.001}$ alloy. The short- and long-dashed lines are straight-line fits to the plotted points for $\alpha = 0°$ and $\alpha = 55°$, respectively. Larger W film thicknesses are needed for detectability of the W 4d$_{5/2}$ peak when the W film is buried at larger depths in the Ru matrix.

of survey scans, protocols for narrow scans and analysis of results, identification of chemical state and sample morphology, and quantitative analyses. These recommendations, which are slowly being adopted, are a valuable source of "best practices" as well as an educational resource for both novice and experienced analysts.

Reference procedures (that is, documentary standards) for surface analysis have been developed by ASTM International Committee E-42 on Surface Analysis [21] and by Technical Committee 201 on Surface Chemical Analysis of the International Organization for Standardization (ISO) [22]. These standards provide recommended terminology and definitions, procedures for handling and mounting specimens, procedures to calibrate and check the performance of XPS and other instruments, and information on how to acquire, analyze, and interpret XPS and other spectra. ASTM and ISO standards are also available for the other common methods of surface analysis and for data transfer and information formats to be used in surface analysis [21,22].

Conclusion

The use of XPS has grown considerably during the past 25 years, indicating the wide utility of this method of surface analysis. This growth has occurred in part as the result of the development of new instrumental capabilities, the development of advanced materials for new technologies, and growing developments in nanoscience and bio-applications. Seven NIST databases are now available that provide needed data for quantitative applications of XPS. The NIST SESSA database provides not only data for quantitative XPS analyses, but the ability to simulate XPS spectra for complex samples such as multilayer-film stacks on a planar substrate and nanostructures such as islands, lines, spheres, and layered spheres on a substrate.

Acknowledgments

I thank Dr. D. R. Baer, Dr. S. B. Hill, and Dr. C. E. Lyman for their useful suggestions for improving the manuscript.

References

[1] VS Smentkowski, *Microscopy Today* 19 (2011) 10.
[2] CR Brundle et al., *J Electron Spectrosc Relat Phenom* 178/179 (2010) 433–48.
[3] DR Baer et al., *J Vac Sci Technol A* 31 (2013) 050820.
[4] D Briggs and JT Grant. (eds.), *Surface Analysis by Auger and X-ray Photoelectron Spectroscopy*. IM Publications, Chichester, 2003.
[5] JC Vickerman and IS Gilmore. (eds.), *Surface Analysis: The Principal Techniques* (second edition), Wiley, Chichester, 2009.
[6] S Hofmann, *Auger- and X-ray Photoelectron Spectroscopy in Materials Science*. Springer, Heidelberg, 2013.
[7] National Institute of Standards and Technology (NIST), "Surface Data," http://www.nist.gov/srd/surface.cfm.
[8] CJ Powell and A Jablonski, *Nucl Instr Meth Phys Res A* 601 (2009) 54–65.
[9] H Shinotsuka et al., *Surf Interface Anal* 47 (2015) 871–88.
[10] X Llovet et al., *J Phys Chem Ref Data* 43 (2014) 013102.
[11] NIST, "X-ray Transition Energies," http://www.nist.gov/pml/data/xraytrans/index.cfm.
[12] NIST, "Note on the X-Ray Attenuation Databases," http://physics.nist.gov/PhysRefData/XrayNoteB.html.
[13] M Mohai, *Surf Interface Anal* 36 (2004) 828–32; M Mohai, "XPS MultiQuant for Windows," http://aki.ttk.mta.hu/XMQpages/XMQhome.htm.
[14] S Tougaard, *J Vac Sci Technol A* 14 (1996) 1415–23.
[15] S Tougaard, *J Electron Spectrosc Relat Phenom* 178/179 (2010) 128–53; QUASES-Tougaard Inc., "QUASES: Software packages to characterize surface nano-structures by analysis of electron spectra," http://www.quases.com.
[16] A commercial product is identified to indicate a type of available software. This identification does not imply that the product is endorsed or recommended by the National Institute of Standards and Technology or that the product is necessarily the most suitable for the purposes described.
[17] W Smekal et al., *Surf Interface Anal* 37 (2005) 1059–67; NIST, "NIST Standard Reference Database 100," http://www.nist.gov/srd/nist100.cfm.
[18] NS Faradzhev, SB Hill and CJ Powell. (to be published).
[19] CJ Powell et al., *J Vac Sci Technol A* 32 (2014) 050603.
[20] JE Castle and CJ Powell, *Surf Interface Anal* 36 (2004) 225–37; IUVSTA, "Reports of the 34th IUVSTA Workshop," http://www.iuvsta.org/W34.html.
[21] ASTM International, "Committee E42 on Surface Analysis," http://www.astm.org/COMMITTEE/E42.htm.
[22] CJ Powell, *Surf Interface Anal* 47 (2015) 127–34; International Organization for Standardization, http://www.iso.org.

MT